

Giant anomalous Nernst effect in the magnetic Weyl semimetal $\text{Co}_3\text{Sn}_2\text{S}_2$

Haiyang Yang,¹ Wei You,¹ Jialu Wang,¹ Junwu Huang,¹ Chuanying Xi,² Xiaofeng Xu,³ Chao Cao,^{1,*}
Mingliang Tian,² Zhu-An Xu,⁴ Jianhui Dai,^{1,†} and Yuke Li^{1,‡}

¹Department of Physics and Hangzhou Key Laboratory of Quantum Matters, Hangzhou Normal University, Hangzhou 311121, China

²High Magnetic Field Laboratory, Chinese Academy of Sciences, Hefei 230031, China

³Department of Physics, Changshu Institute of Technology, Changshu 215500, China

⁴Zhejiang Province Key Laboratory of Quantum Technology and Device and Department of Physics, Zhejiang University, Hangzhou 310027, China



(Received 10 January 2019; revised manuscript received 7 December 2019; accepted 17 January 2020; published 10 February 2020)

In ferromagnetic solids, a transverse voltage can be generated by a longitudinal temperature gradient even in the absence of a magnetic field. This thermoelectric counterpart of the anomalous Hall effect is dubbed the anomalous Nernst effect (ANE), and both of these effects are expected to scale with spontaneous magnetization. Here, we report the observation of a giant ANE in a newly discovered magnetic Weyl semimetal $\text{Co}_3\text{Sn}_2\text{S}_2$ crystal. The Hall effect and the Nernst effect show sharp jumps at a threshold field and exhibit a clear hysteresis loop below the Curie temperature T_C . The anomalous Nernst signal, S_{yx}^A , peaks at a maximum value of $\sim 5 \mu\text{V}/\text{K}$, which is comparable to the largest seen in previous magnetic materials and seriously violates the conventional scale relation in conventional ferromagnets. Moreover, the anomalous transverse thermoelectric conductivity α_{yx}^A reaches about $\sim 10 \text{ A}/\text{K m}$ at 70 K, the largest in known semimetals. These results together with first-principles calculation provide strong evidence that the giant ANE originated from the nontrivial Berry curvature near the chiral Weyl points, which are very close to the Fermi level in this compound.

DOI: [10.1103/PhysRevMaterials.4.024202](https://doi.org/10.1103/PhysRevMaterials.4.024202)

I. INTRODUCTION

The Nernst effect, i.e., the transverse electric field generated by a longitudinal thermal gradient in the presence of a magnetic field, has triggered renewed attention in condensed-matter physics since the discovery of a pseudogap phase in cuprates [1,2]. Since that time, the large Nernst effect has been observed in correlated electron systems [3–5], conventional semimetals [6], as well as metallic ferromagnets [7–9]. Consequently, a number of novel ground states [3] and exotic electronic orders [5,10,11] can be identified by measuring the Nernst effect. For some ferromagnetic metals, in particular, the Nernst signal was observed below T_C even in the absence of an external magnetic field [7–9]. This phenomenon, known as the anomalous Nernst effect (ANE), is observed to be proportional to the magnetization, geometrically connected to the Berry curvature of Bloch bands at the Fermi energy [12]. In spite of many efforts, the maximum value of the ANE in ferromagnets is limited to below $\sim 1 \mu\text{V}/\text{K}$ [13].

In recent years, topological Dirac/Weyl semimetal materials have been theoretically predicted and experimentally discovered. The electronic structures of these materials have topologically robust [14–18] and symmetry-protected bulk energy bands that linearly intersect at some special points (the Dirac points) or symmetry axis near the Fermi level [19,20].

Breaking spatial inversion symmetry or time-reversal symmetry (TRS) can split a Dirac point into a pair of the Weyl points with opposite chiralities. The chiral Weyl points are then the source or the sink of Berry curvature $\Omega(k)$ [21], meaning that the Berry curvature is singular at these points [22]. Dozens of Dirac/Weyl semimetals have been investigated [23–30], and several phenomena such as the large magnetoresistivity (MR) [30] and ultrahigh mobility [24] have been observed. However, the defining properties of such topological semimetals, including the Fermi arc in surface states and chiral anomaly in charge transports, are not easy to identify experimentally. So far, angle-resolved photoemission spectroscopy (ARPES) measurements have been established as direct evidence of the Fermi arc in the TaAs family [31,32], while a possible indirect signature of the chiral anomaly is associated with the negative longitudinal MR as investigated in several relevant materials [27,33,34]. However, it is difficult to rule out some extrinsic factors such as the current jetting effect and crystal inhomogeneity [35].

Quite interestingly, two kinds of transverse transport properties—the anomalous Hall effect (AHE) and the ANE—can help to probe the topological nature of charge carriers in magnetic Weyl semimetals (MWSs). This is because both the AHE and the ANE are mainly contributed from the intrinsic magnetic field and are thus deemed as strong proof of the finite Berry curvature originating from the separated Weyl nodes [36]. Recently, the AHE [37,38] was observed in a MWS $\text{Co}_3\text{Sn}_2\text{S}_2$ compound with a kagome lattice. The magnetic kagome lattice due to its unusual symmetry and geometrical frustration usually provides an excellent platform

*ccao@hznu.edu.cn

†daijh@hznu.edu.cn

‡yklee@hznu.edu.cn

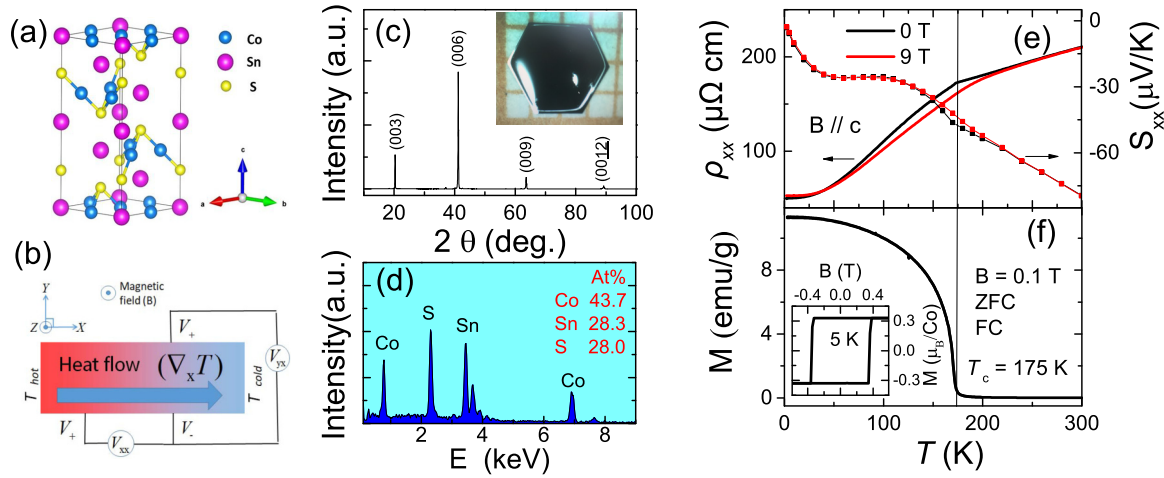


FIG. 1. Crystal structure, XRD diffraction, resistivity, and magnetization of $\text{Co}_3\text{Sn}_2\text{S}_2$. (a) The crystal structure of $\text{Co}_3\text{Sn}_2\text{S}_2$. (b) A schematic diagram of the thermal-electrical measurements (Seebeck and Nernst effects). In this geometry, a temperature gradient $\nabla_x T$ produces a transverse thermoelectric voltage V_{yx} in a magnetic field. (c) The XRD patterns at room temperature and a photograph of the single crystal. (d) The EDX spectroscopy of single crystal. (e) Temperature dependence of longitudinal electric resistivity (left), ρ_{xx} , and thermopower (right), S_{xx} , of the $\text{Co}_3\text{Sn}_2\text{S}_2$ sample under zero field and 9 T. (f) Temperature dependence of magnetization with the zero-field-cooling (ZFC) and field-cooling (FC) modes at $B = 0.1$ T. The inset shows the saturated magnetization vs fields at 5 K.

for exotic topological states such as spin liquids and magnetic skyrmions, and for various anomalous transports. Such a feature is actually not observed in other topological magnetic semimetals, such as Co_2MnGa [39] and Mn_3Sn [40], which exhibit the AHE and the ANE. Thus, it is highly desirable to investigate the ANE, the thermoelectric counterpart of the AHE, in the rare ferromagnetic Weyl semimetal $\text{Co}_3\text{Sn}_2\text{S}_2$, and then reveal the origin of the anomalous transport behaviors, which also remain to be clarified in the various MWS systems. In addition, unlike the Hall effect where the normal contribution in a metal is always finite, the Nernst effect generally vanishes in ordinary metals due to the Sondheimer cancellation [41], implying that the anomalous contribution may become very prominent. Another noticeable fact is that a large AHE does not necessarily imply a large ANE. This is because the AHE is contributed from the sum of Berry curvatures of all occupied bands, while the ANE is governed by the Berry curvature close to the Fermi level [12,42]. Thus, studying the ANE is necessary to confirm the Berry curvature contribution and in turn to verify the intrinsic Weyl state in Weyl semimetals.

In this paper, we systematically study the ANE in the magnetic Weyl semimetal $\text{Co}_3\text{Sn}_2\text{S}_2$. We find that the anomalous Nernst signal (ANS) reaches a maximum value of $\sim 5 \mu\text{V}/\text{K}$ at 70 K, yielding a giant anomalous transverse thermoelectrical conductivity (ATTG) of $\sim 10 \text{ A}/\text{K m}$, much larger than those of known ferromagnetic metals. The observed giant ANS is largely beyond the conventional scale relation in ferromagnets. Our experimental studies together with first-principles calculation also provide helpful insights into the intrinsic Weyl state and the correlation between AHE and ANE.

II. EXPERIMENTAL DETAILS

Large single crystals of $\text{Co}_3\text{Sn}_2\text{S}_2$ with the millimeter size were grown through the Bridgman technique, as reported

in the literature [43]. The crystal x-ray diffraction patterns were performed using a D/MaxrA diffractometer with $\text{Cu K}\alpha$ radiation at 300 K, which determines the crystal orientations. Only the (00l) Bragg peaks [Fig. 1(c)] are clearly observed, demonstrating that the exposed surface is an *ab* plane. A picture of a $3.5 \times 3 \times 0.2 \text{ mm}^3$ single crystal is shown in the inset of Fig. 1(c), showing the hexagonal platelike shape. The composition of the crystals was confirmed by energy-dispersive x-ray (EDX) spectroscopy in Fig. 1(d), showing that the ratio of Co, Sn, and S in our samples is very close to 3 : 2 : 2. $\text{Co}_3\text{Sn}_2\text{S}_2$ crystallizes in a rhombohedral structure with the space group of $R\bar{3}m$, and consists of a quasi-two-dimensional Co_3Sn layer sandwiched between sulfur atoms. Co atoms form a kagome lattice with corner-sharing triangles of Co atoms in the CoSn -layer, and the kagome lattices in different layers are stacked along the *c*-axis with a corner-sharing octahedra [Fig. 1(a)].

The measuring crystals are polished and then cut into a bar shape. The (magneto)resistivity and Hall coefficient measurements were performed using the standard four-terminal method in a commercial Quantum Design PPMS-9 system. The magnetization measurements were done using a commercial SQUID magnetometer. The thermoelectric effects including thermopower and the Nernst effect were performed with a one-heater–two-thermometers technique in a physical property measurement system (PPMS) with a high-vacuum environment. All transport experiments are performed using two kinds of measuring configurations, as shown in Fig. 1(b): The longitudinal measurements involve the resistivity and the thermopower, where the electric voltage is parallel to electrical current or heat flow. The corresponding physical quantities are marked with the subscript *xx*, and the transverse measurements include the Hall effect and the Nernst effect, where the electric voltage is normal to the electrical current or the thermal gradient. Correspondingly, the physical parameters are marked with the subscript *yx*. To fully understand the experimental results, we also performed the *ab initio*

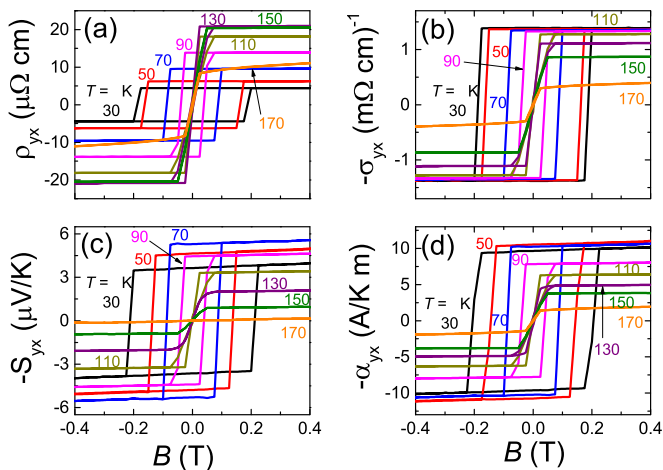


FIG. 2. Field dependence of transport coefficients at several temperatures as $B \parallel c$ -axis $\perp I$. (a) Hall resistivity ρ_{yx} vs magnetic fields. (b) The Hall conductivity $-\sigma_{yx}$, extracted from ρ_{xx} and ρ_{yx} . (c) The Nernst signal $-S_{yx}$ as a function of magnetic field. (d) Transverse thermoelectric conductivity $-\alpha_{yx}$, extracted from ρ_{xx} , ρ_{yx} , S_{xx} , and S_{yx} . The hysteretic behavior is clearly observed at low temperatures.

calculations using density-functional theory [see the supplementary information (SI) I [44]].

For the thermoelectric effect measurements, two Chromel-constantan (type E) thermocouples were employed to measure the temperature gradient generated by a small heater chip, and thermal contacts were accomplished via gold wires. The distance of the thermometers (L_x) is ~ 2 mm in our measurements. With the increase in sample temperature, the temperature gradient increases correspondingly by increasing the current of resistivity heater. In the Nernst effect measurements, a slight misalignment of the voltage contacts can give rise to an extra contribution associated with the longitudinal signals (i.e., thermopower S_{xx}). However, the Nernst effect is generally field-odd while the thermopower is field-even, therefore such a contribution can be canceled by reversing the direction of the magnetic field during measurements.

Here, we remark that the Nernst signal $S_{yx} = \frac{E_y}{\nabla_x T} = \frac{V_{yx}}{\delta T} \frac{L_x}{L_y}$ can be obtained from the observed transverse voltage difference (V_{yx}), the temperature difference (δT), and the ratio of $\frac{L_x}{L_y}$, where L_y is the distance of transverse voltage contacts. In addition, in our manuscript these physical quantities— $\rho_{yx}^A/\sigma_{yx}^A$, S_{yx}^A , and α_{yx}^A —represent the anomalous Hall resistivity/conductivity (AHR/AHC), the anomalous Nernst signal (ANS), and the anomalous transverse thermoelectric conductivity (ATTC), respectively, where the superscript A stands for ‘‘anomalous.’’ ρ_{yx}^A , σ_{yx}^A , S_{yx}^A , and α_{yx}^A can be obtained by extrapolating the high-field part of ρ_{yx} , σ_{yx} , S_{yx} , and α_{yx} back to zero field, respectively, as shown in Fig. 2.

III. RESULTS AND DISCUSSION

$\text{Co}_3\text{Sn}_2\text{S}_2$ shows a magnetic moment of $\sim 0.33\mu_B/\text{Co}$ along the c -axis with a Néel temperature of about 175 K [Fig. 1(f)]. The FC and ZFC curves overlap each other very well at 0.1 T, implying that the magnetic domains have been arranged along the c -axis by small external fields. A clear hys-

teresis loop with a saturated magnetization M_s of $0.33\mu_B/\text{Co}$ at 5 K is observed in the inset of Fig. 1(f), in agreement with the theoretical prediction [37,38]. The temperature dependence of longitudinal resistivity ρ_{xx} and the thermopower S_{xx} of $\text{Co}_3\text{Sn}_2\text{S}_2$ are shown in Fig. 1(e). Overall, the resistivity shows a metallic behavior in the whole temperature region with an unexpected kink associated with a ferromagnetic transition (FM) at about $T_c = 175$ K, similar to the previous report [43]. Applying a magnetic field up to 9 T, the resistivity does not change too much at high temperature but starts to decrease below 200 K. The kink in $\rho_{xx}(T)$ near T_c broadens and becomes very smooth under 9 T, as seen in the literature [37,38]. The zero-field thermopower, S_{xx} , is negative and shows a strong temperature dependence in the measuring temperature range. Upon cooling the temperature from 300 K, it decreases linearly and then shows a similar kink near T_c , similar to that previously reported in the polycrystal [45]. The applied magnetic field (9 T) seriously suppresses the kink at around T_c , but does not affect the S_{xx} in magnitude in the other temperature regions, consistent with the behavior of resistivity.

Figures 2(a) and 2(c) display the Hall resistivity ρ_{yx} and the Nernst signal $-S_{yx}$ versus the applied magnetic fields $B \parallel c \perp I$ at several representative temperatures below T_c . $\rho_{yx}(B)$ significantly exhibits a steep rectangular hysteretic jump at low fields, and then becomes almost flat at higher fields, consistent with the typical ones for ferromagnets. Its magnitude is comparable to the previous results [37,38]. As the temperature rises, the coercive field gradually decreases and then vanishes until the Curie temperature. Similarly, the significant $S_{yx}(B)$ (here the Nernst effect caused by vortex motion is positive) also shows hysteretic jumps at different temperatures and then becomes a constant at high fields, as shown in Fig. 2(c). A maximum value of S_{yx} about $5 \mu\text{V}/\text{K}$ is observed at 70 K, which is over one order of magnitude larger than those in typical materials such as Mn_3Sn [46], the pure metal Fe [47], $\text{CuCr}_2\text{Se}_{4-x}\text{Br}_x$ [8], and the single crystal Fe_3O_4 [9]. Upon further warming the temperature, the S_{yx} starts to decrease and finally approaches zero as $T > T_c$. Note that both the Hall resistivity and the Nernst signal show nearly the same field dependence similar to the magnetization curve (see the SI, Fig. S1 [44]), implying that the contribution of the anomalous Hall and Nernst effects dominates and the normal contribution (proportional to B) is negligibly small at low fields.

The field dependence of the Hall conductivity $-\sigma_{yx}$ and the transverse thermoelectric conductivity $-\alpha_{yx}$ at several representative temperatures are shown in Figs. 2(b) and 2(d). σ_{yx} and α_{yx} can be evaluated using the formulas $\sigma_{yx} = -\rho_{yx}/(\rho_{yx}^2 + \rho_{xx}^2)$ and $\alpha_{yx} = (\rho_{xx}S_{yx} - \rho_{yx}S_{xx})/(\rho_{xx}^2 + \rho_{yx}^2)$ [47] (here $\rho_{xx} = \rho_{yy}$ and $S_{xx} = S_{yy}$, see SI Fig. S6 [44]). Overall, both σ_{yx} and α_{yx} curves show a similar rectangular hysteretic jump at low fields, corresponding to the data of Hall resistivity and the Nernst signal, respectively. The derived $|\sigma_{yx}|$ reaches $\sim 1270 (\Omega \text{ cm})^{-1}$ at low temperatures, which is very close to the previous report [$1130 (\Omega \text{ cm})^{-1}$] in the same system [37,38]. Surprisingly, the obtained $|\alpha_{yx}|$ is found to be very large, reaching approximately $10 \text{ A}/\text{K m}$ at 70 K. This value is one or two orders of magnitude larger than typical ferromagnets such as Mn_3Sn , which has $\alpha_{yx} \sim 0.01\text{--}1 \text{ A}/\text{K m}$ [see Fig. 4(c) and SI Fig. S3 [44]].

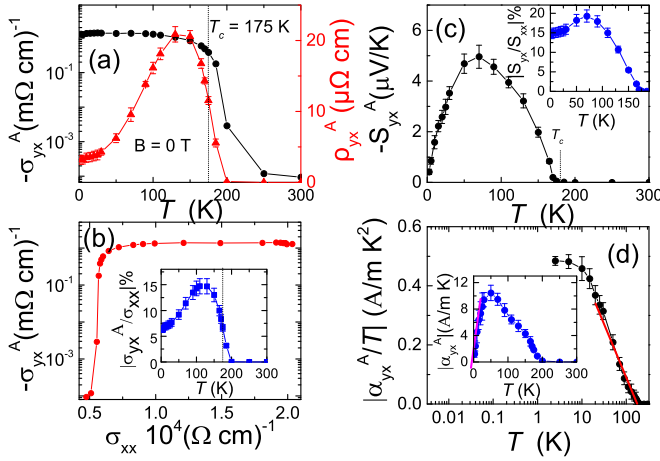


FIG. 3. Temperature dependence of transport coefficients in $\text{Co}_3\text{Sn}_2\text{S}_2$. (a) Temperature dependence of the anomalous Hall conductivity $-\sigma_{yx}^A$ and Hall resistivity ρ_{yx}^A at zero magnetic field. (b) $-\sigma_{yx}^A$ as a function of σ_{xx} in the main panel. The inset shows the temperature dependence of the Hall angle ($|\sigma_{yx}^A/\sigma_{xx}|$) at zero magnetic field. (c) Temperature dependence of the anomalous Nernst signal S_{yx}^A . The inset shows the Nernst angle $|\theta_N = S_{yx}^A/S_{xx}|$ as a function of temperature. (d) Temperature dependence of the $|\alpha_{yx}^A|/T$. The inset shows the transverse thermoelectric conductivity α_{yx} vs temperature.

The temperature dependence of the anomalous Hall resistivity (AHR), ρ_{yx}^A , and the anomalous Hall conductivity (AHC), $-\sigma_{yx}^A$, are illustrated in Fig. 3(a). ρ_{yx}^A shows a strong temperature dependence below T_c , and it peaks at a maximum value of $21 \mu\Omega \text{ cm}$ around 140 K, while σ_{yx}^A is almost temperature-independent below 100 K. Such a feature was observed in pure materials such as Fe, Co, Ni, and Gd, where this effect is ascribed to the intrinsic Berry phase [7]. We plot $-\sigma_{yx}^A$ as a function of σ_{xx} in the main panel of Fig. 3(b). $-\sigma_{yx}^A$ is weakly dependent on σ_{xx} in the low-temperature regime (<100 K), similar to the case in Fe, Ni pure metals [7] (see Fig. S3 in the SI). A large anomalous Hall angle $|\sigma_{yx}^A/\sigma_{xx}|$ reaches a maximum value about 15% at 150 K and gradually decreases to 6.3% at 5 K [shown in the inset of Fig. 3(b)]. The large Hall angle in $\text{Co}_3\text{Sn}_2\text{S}_2$ is close to the value of 16% in GdPtBi, a typical field-induced Weyl semimetal [48], and is larger than those of the noncollinear antiferromagnetic Mn_3Sn (3.2%) [40] and Mn_3Ge (5%) [46].

The anomalous Nernst signal (ANS) $-S_{yx}^A$ as a function of temperature in Fig. 3(c) is displayed. $-S_{yx}^A$ depends strongly on temperature, rapidly increases below T_c , and then peaks at around 70 K, half of the peak temperature of ρ_{yx}^A in Fig. 3(a). Similar to the large Hall angle, large S_{yx}^A can be verified by the Nernst angle $\theta_N = |S_{yx}^A/S_{xx}|$ in the inset of Fig. 3(c). The value reaches 17% at 70 K, which is comparable with the previous findings in the Co_2MnGa system [39,49], a FM semimetal. Correspondingly, the temperature dependence of $|\alpha_{yx}^A|$ is mapped in the inset of Fig. 3(d), and $|\alpha_{yx}^A|$ rapidly increases below 200 K, showing a maximum value of ~ 11 A/K m at 50 K, followed by a monotonous decrease to low temperatures. Such a large α_{yx}^A is one or two orders of magnitude larger than other ferromagnets, which usually show $\alpha_{yx}^A \sim 0.01\text{--}1$ A/K m [see Fig. 4(c)]. Note that α_{yx}^A roughly

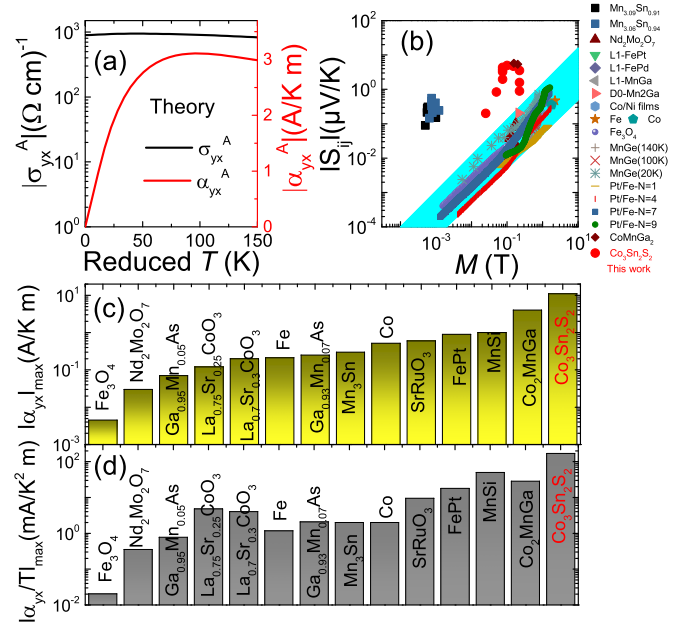


FIG. 4. The ANE of $\text{Co}_3\text{Sn}_2\text{S}_2$ in theoretical calculations, Mn_3Sn , and ferromagnets in experimental results. (a) Temperature dependence of the theoretically calculated AHC and TTC at a fixed Fermi level. (b) Magnetization dependence of the spontaneous Nernst effect for FM metals, Mn_3Sn and $\text{Co}_3\text{Sn}_2\text{S}_2$. (c) The transverse thermoelectric conductivity (TTC) $|\alpha_{yx}|$ vs the various ferromagnets, Mn_3Sn and $\text{Co}_3\text{Sn}_2\text{S}_2$. (d) $|\alpha_{yx}|/T$ vs the various ferromagnets, Mn_3Sn and $\text{Co}_3\text{Sn}_2\text{S}_2$. All those ANE results are obtained for various ferromagnets below their Curie temperatures. (More details of Fig. 4 can be seen in the SI [44].)

obeys the linear T -dependence at low temperatures, while it closely follows the relation $\propto T \ln(T)$ at a temperature regime from 70 to 175 K as shown in the main panel of Fig. 3(d). A similar feature has been reported in a Co_2MnGa system [39], but evidence of the Lifshitz transition at finite temperature was not observed in our sample.

To understand the large intrinsic AHC and ATTC, as well as their temperature dependence, we have performed first-principles calculations. Assuming the magnetic moment is along the z -direction, the calculation yields a total magnetic moment of $1\mu_B$ per unit cell, or $0.33\mu_B/\text{Co}$. The inclusion of spin-orbit coupling (SOC) lifts the twofold degeneracy along a nodal ring around the L point, leaving only two Weyl points (see SI Fig. S4 [44]). These results are in good agreement with previous calculations [37,38]. We then fitted the first-principles results to the 62-orbital tight-binding model considering Co $3d$, Sn $5s$, Sn $5p$, S $2s$, and S $2p$ orbitals using the Wannier projection method [50]. σ_{yx}^A and α_{yx}^A are then evaluated using a semiclassical approach [42]:

$$\sigma_{yx}^A = -\frac{e^2}{\hbar} \int \frac{dk}{2\pi^3} \Omega_{n,z}(k) f_{nk}$$

and

$$\alpha_{yx}^A = -\frac{e}{T\hbar} \int \frac{dk}{2\pi^3} \Omega_{n,z}(k) s_{nk},$$

$$s_{nk} = (\varepsilon_{n,k} - \mu) f_{n,k} + k_B T \ln[1 + e^{-\beta(\varepsilon_{n,k} - \mu)}],$$

where $\Omega_{n,k}$ is the Berry curvature along the z -direction, and $f_{nk} = f(\varepsilon_{n,k})$ is the Fermi distribution function with the band index n and the wave vector k . $\varepsilon_{n,k}$ and β denote the band energy and $1/k_B T$. The second formula can be transformed to a more symmetric form: $\alpha_{yx}^A = -\frac{e}{T\hbar} \int \frac{dk}{2\pi^3} \Omega_{n,z}(k) g_{nk}$, where $g_{nk} = f_{nk} \ln f_{nk} + (1 - f_{nk}) \ln(1 - f_{nk})$. At zero temperature, f_{nk} becomes a step function, thus $g_{nk} \equiv 0$ and α_{yx}^A is always 0 at 0 K, while σ_{yx}^A depends on the summation of Berry curvature of all occupied bands, which yields $\sigma_{yx}^A = 1230$ S/cm for a pristine compound.

The temperature dependence may be further understood by dividing the whole temperature range into two parts. At low temperatures when the ferromagnetic phase is robust, we can ignore the temperature dependence of the band structure. Thus the temperature dependence is completely due to the Fermi-Dirac distribution f_{nk} . However, since the DFT band structure usually overestimates the bandwidth, and f_{nk} only depends on the ratio between the state energy and temperature, we renormalized our band energies using the ratio $\gamma_{\text{exp}}/\gamma_{\text{cal}} = 3.55$, where γ denotes the electron specific-heat coefficient, γ_{exp} is obtained from experiment (see SI Fig. S2 [44]), and γ_{cal} is the value derived from the DFT density of states. The resulting σ_{yx}^A and α_{yx}^A bear a remarkable resemblance to the experimental results. Overall, the ATTC linearly increases at low temperature and shows a peak at about 70 K that is also observed in the experiment. The theoretical maximum $\alpha_{yx}^A \sim 3.5$ A/K m is somewhat smaller than the experimental value, possibly due to effects beyond the current considerations, including the temperature dependence of the magnetic moments (see SI Fig. S5 [44]). Nevertheless the ANE should share a common origin related to the Berry curvature effect with the AHE as the Nernst signal does not follow the conventional scaling relation [see Fig. 4(b)] either. Moreover, the ATTC depends sensitively on the contribution of the Berry curvature when the Weyl points are very close to the Fermi energy. Therefore, the observed large values of ATTC, as well as the same characteristic T -dependence of α_{yx}^A in experiment and calculation, are all beyond the conventional mechanism for the ANE in ferromagnets and can be deemed as the main contribution of Berry curvature associated with the emerging Weyl points in the present system. At high temperatures close to the FM to PM phase transition, the previous assumption no longer holds, and the temperature dependence will be dominated by the Berry curvature change due to a phase transition. This leads to the sudden drop of the AHE, as well as the disappearance of the ANE. Of course, both the skew scatter and the side jump contribution to the ANE have been suggested before [51,52]. Here, the skew scatter is expected to appear in the extremely pure sample with very high conductivity (10^6 S/cm), thus it is simply ruled out in our sample. The side jump is hard to distinguish due to the independence of the quasiparticle scattering rate, but its contribution to the ANE is found to be small in some ferromagnets [52]. Thus, the extrinsic scatter contribution may play a minor role in the ANE in our case.

Further declaring such a large ATTC in $\text{Co}_3\text{Sn}_2\text{S}_2$ different from the conventional ferromagnets, we compare in Fig. 4(b) the significant difference between the giant ANE in $\text{Co}_3\text{Sn}_2\text{S}_2$, Mn_3Sn , and in ferromagnets. We plot the absolute value of the ANE as functions of the magnetization with a logarithmic

scale for various ferromagnetic metals, Mn_3Sn and $\text{Co}_3\text{Sn}_2\text{S}_2$. The ANE in ferromagnets is known to be roughly proportional to the magnetization M , $|S_{yx}^A| = |Q_s| \mu_0 M$, where $|Q_s|$ is the anomalous Nernst coefficient. It can be seen that almost all ferromagnetic metals follow this relation, and their anomalous Nernst signal S_{yx}^A becomes larger with increasing magnetization. The shaded region covers all of the data points for ferromagnets. According to the above scaling relation, the expected S_{yx}^A value for $\text{Co}_3\text{Sn}_2\text{S}_2$ at 70 K is about 0.006–0.2 $\mu\text{V/K}$. The observed S_{yx}^A is far away from this trend and more than one or two orders of magnitude larger than what would be expected based on the scaling relation, indicating that the anomalous Nernst signal in $\text{Co}_3\text{Sn}_2\text{S}_2$ arises from a different mechanism than the ANE in conventional ferromagnets. Note that another exception for the antiferromagnetic Mn_3Sn observed strongly violates this scaling, which is ascribed to the enhanced Berry curvature at the Fermi energy [40]. Correspondingly, the intrinsic transverse thermoelectric conductivity $|\alpha_{yx}^A|$ is close to 10.6 A/K m for $\text{Co}_3\text{Sn}_2\text{S}_2$, the largest value compared to the other ferromagnets and semimetals as shown in Fig. 4(c). Based on the Mott relation $\frac{\alpha_{yx}^A}{T} = -\frac{\pi^2 k_B^2}{3e} \left[\frac{d\sigma_{xy}}{d\varepsilon} \right]_{\mu}$, α_{yx}^A/T is proportional to the energy derivative of the AHE. Below T_c , the ferromagnetic transition induces the modification of the band structures at the Fermi level, leading to a sharp decrease of carrier density at a temperature regime. Thus, α_{yx}^A/T still shows the largest values compared to the other conventional ferromagnets and semimetals [see Fig. 4(d)]. However, the more complicated physics is hard to understand based on our present experimental data. More measurements should be performed to investigate this issue, such as ARPES.

IV. CONCLUSION

In summary, we report an observation of the giant ANE and large intrinsic transverse thermoelectric conductivity in the magnetic Weyl semimetal $\text{Co}_3\text{Sn}_2\text{S}_2$. The Nernst signal S_{yx} reaches ~ 5 $\mu\text{V/K}$ at 70 K, much larger than those of known ferromagnetic metals. Furthermore, the $\alpha_{yx}^A \sim 10$ A/K m is over one or two orders of magnitude larger than those of other ferromagnets where $\alpha_{yx}^A = 0.01$ –1 A/K m. Our experimental results together with the first-principles calculations indicate that the giant ANE in $\text{Co}_3\text{Sn}_2\text{S}_2$ can be ascribed to the enhanced contribution from the Berry curvature very close to the Fermi level in this compound. Our experimental results also highlight the complementary roles of the ANE and the AHE in revealing the intrinsic Weyl states in magnetic Weyl semimetals.

ACKNOWLEDGMENTS

We thank K. Behnia for inspiring discussions and suggestions. We also thank H. Wang and J. Yang for some technical support. This research was supported in part by the NSF of China (under Grants No. 11474082, No. 11874136, No. 11874137, No. U1932155, and No. U1732274) and the National Key Projects for Research and Development of China (Contract No. 2016YFA0300402). Y.-K.L. was supported by an open program from Wuhan National High Magnetic Field Center (2016KF03).

- [1] Z. A. Xu, N. P. Ong, Y. Y. Wang, T. Kakeshita, and S. Uchida, *Nature (London)* **406**, 486 (2000).
- [2] Y. Y. Wang, L. Li, and N. P. Ong, *Phys. Rev. B* **73**, 024510 (2006).
- [3] K. Behnia, *J. Phys.: Condens. Matter* **21**, 113101 (2009).
- [4] R. Bel, K. Behnia, Y. Nakajima, K. Izawa, Y. Matsuda, H. Shishido, R. Settai, and Y. Onuki, *Phys. Rev. Lett.* **92**, 217002 (2004).
- [5] R. Bel, H. Jin, K. Behnia, J. Flouquet, and P. Lejay, *Phys. Rev. B* **70**, 220501(R) (2004).
- [6] K. Behnia, M.-A. Méasson, and Y. Kopelevich, *Phys. Rev. Lett.* **98**, 076603 (2007).
- [7] T. Miyasato, N. Abe, T. Fujii, A. Asamitsu, S. Onoda, Y. Onose, N. Nagaosa, and Y. Tokura, *Phys. Rev. Lett.* **99**, 086602 (2007).
- [8] W. L. Lee, S. Watauchi, V. L. Miller, R. J. Cava, and N. P. Ong, *Phys. Rev. Lett.* **93**, 226601 (2004).
- [9] R. Ramos, M. H. Aguirre, A. Anadon, J. Blasco, I. Lucas, K. Uchida, P. A. Algarabel, L. Morellon, E. Saitoh, and M. R. Ibarra, *Phys. Rev. B* **90**, 054422 (2014).
- [10] A. Pourret, K. Behnia, D. Kikuchi, Y. Aoki, H. Sugawara, and H. Sato, *Phys. Rev. Lett.* **96**, 176402 (2006).
- [11] O. Cyr-Choinière, R. Daou, F. Laliberté, D. LeBoeuf, N. Doiron-Leyraud, J. Chang, J.-Q. Yan, J.-G. Cheng, J.-S. Zhou, J. B. Goodenough, S. Pyon, T. Takayama, H. Takagi, Y. Tanaka, and L. Taillefer, *Nature (London)* **458**, 743 (2009).
- [12] D. Xiao, Y. G. Yao, Z. Fang, and Q. Niu, *Phys. Rev. Lett.* **97**, 026603 (2006).
- [13] J. P. Perdew, K. Burke, and M. Ernzerhof, *Phys. Rev. Lett.* **77**, 3865 (1996).
- [14] N. P. Armitage, E. J. Mele, and A. Vishwanath, *Rev. Mod. Phys.* **90**, 015001 (2018).
- [15] X. Wan, A. M. Turner, A. Vishwanath, and S. Y. Savrasov, *Phys. Rev. B* **83**, 205101 (2011).
- [16] S. M. Young, S. Zaheer, J. C. Y. Teo, C. L. Kane, E. J. Mele, and A. M. Rappe, *Phys. Rev. Lett.* **108**, 140405 (2012).
- [17] K. Y. Yang, Y. M. Lu, and Y. Ran, *Phys. Rev. B* **84**, 075129 (2011).
- [18] C. Fang, M. J. Gilbert, X. Dai, and B. A. Bernevig, *Phys. Rev. Lett.* **108**, 266802 (2012).
- [19] A. A. Burkov, M. D. Hook, and L. Balents, *Phys. Rev. B* **84**, 235126 (2011).
- [20] G. Xu, H. M. Weng, Z. J. Wang, X. Dai, and Z. Fang, *Phys. Rev. Lett.* **107**, 186806 (2011).
- [21] S. Murakami and S. I. Kuga, *Phys. Rev. B* **78**, 165313 (2008).
- [22] Z. Fang, N. Nagaosa, K. S. Takahashi, A. Asamitsu, R. Mathieu, T. Ogasawara, H. Yamada, M. Kawasaki, Y. Tokura, and K. Terakura, *Science* **302**, 92 (2003).
- [23] Z. J. Wang, H. M. Weng, Q. S. Wu, X. Dai, and Z. Fang, *Phys. Rev. B* **88**, 125427 (2013).
- [24] T. Liang, Q. Gibson, M. N. Ali, M. Liu, R. J. Cava, and N. P. Ong, *Nat. Mater.* **14**, 280 (2015).
- [25] Z. Wang, Y. Sun, X.-Q. Chen, C. Franchini, G. Xu, H. Weng, X. Dai, and Z. Fang, *Phys. Rev. B* **85**, 195320 (2012).
- [26] H. M. Weng, C. Fang, Z. Fang, B. A. Bernevig, and X. Dai, *Phys. Rev. X* **5**, 011029 (2015).
- [27] F. Arnold, C. Shekhar, S. C. Wu, Y. Sun, R. D. Reis, N. Kumar, M. Naumann, M. O. Ajeesh, M. Schmidt, A. G. Grushin, J. H. Bardarson, M. Baenitz, D. Sokolov, H. Borrmann, M. Nicklas, C. Felser, E. Hassinger, and B. Yan, *Nat. Commun.* **7**, 11615 (2016).
- [28] C. Shekhar, A. K. Nayak, Y. Sun, M. Schmidt, M. Nicklas, I. Leermakers, U. Zeitler, Y. Skourski, J. Wosnitza, Z. K. Liu, Y. L. Chen, W. Schnelle, H. Borrmann, Y. Grin, C. Felser, and B. H. Yan, *Nat. Phys.* **11**, 645 (2015).
- [29] N. J. Ghimire, Y. K. Luo, M. Neupane, D. J. Williams, E. D. Bauer, and F. Ronning, *J. Phys.: Condens. Matter* **27**, 152201 (2015).
- [30] C. L. Zhang, Z. J. Yuan, Q. D. Jiang, B. B. Tong, C. Zhang, X. C. Xie, and S. Jia, *Phys. Rev. B* **95**, 085202 (2017).
- [31] S. M. Huang, S. Y. Xu, I. Belopolski, C. C. Lee, G. Q. Chang, B. K. Wang, N. Alidoust, G. Bian, M. Neupane, C. L. Zhang, S. Jia, A. Bansil, H. Lin, and M. Z. Hasan, *Nat. Commun.* **6**, 7373 (2015).
- [32] S. Y. Xu, I. Belopolski, N. Alidoust, M. Neupane, G. Bian, C. L. Zhang, R. Sankar, G. Q. Chang, Z. J. Yuan, C. C. Lee, S. M. Huang, H. Zheng, J. Ma, D. S. Sanchez, B. K. Wang, A. Bansil, F. C. Chou, P. P. Shibayev, H. Lin, S. Jia, and M. Z. Hasan, *Science* **349**, 613 (2015).
- [33] J. Xiong, S. K. Kushwaha, T. Liang, J. W. Krizan, M. Hirschberger, W. D. Wang, R. J. Cava, and N. P. Ong, *Science* **350**, 413 (2015).
- [34] Y. K. Li, L. Li, J. L. Wang, T. T. Wang, X. F. Xu, C. Y. Xi, C. Cao, and J. H. Dai, *Phys. Rev. B* **94**, 121115(R) (2016).
- [35] R. D. Dos Reis, M. O. Ajeesh, N. Kumar, F. Arnold, C. Shekhar, M. Naumann, M. Schmidt, M. Nicklas, and E. Hassinger, *New J. Phys.* **18**, 085006 (2016).
- [36] E. V. Gorbar, V. A. Miransky, I. A. Shovkovy, and P. O. Sukhachov, *Phys. Rev. B* **96**, 155138 (2017).
- [37] E. K. Liu, Y. Sun, N. Kumar, L. Muechler, A. Sun, L. Jiao, S.-Y. Yang, D. F. Liu, A. J. Liang, Q. N. Xu, J. Kroder, V. Süß, H. Borrmann, C. Shekhar, Z. S. Wang, C. Y. Xi, W. H. Wang, W. Schnelle, S. Wirth, Y. L. Chen, S. T. B. Goennenwein, and C. Felser, *Nat. Phys.* **14**, 1125 (2018).
- [38] Q. Wang, Y. F. Xu, R. Lou, Z. H. Liu, M. Li, Y. B. Huang, D. W. Shen, H. M. Weng, S. C. Wang, and H. C. Lei, *Nat. Commun.* **9**, 3681 (2018).
- [39] A. Sakai, Y. P. Mizuta, A. A. Nugroho, R. Sihombing, T. Koretsune, M. T. Suzuki, N. Takemori, R. Ishii, D. N. Hamane, R. Arita, P. Goswami, and S. Nakatsuji, *Nat. Phys.* **14**, 1119 (2018).
- [40] M. Ikhlas, T. Tomita, T. Koretsune, M. T. Suzuki, D. N. Hamane, R. Arita, Y. Otani, and S. Nakatsuji, *Nat. Phys.* **13**, 1085 (2017).
- [41] E. H. Sondheimer, *Proc. R. Soc. London, Ser. A* **193**, 484 (1948).
- [42] D. Xiao, M. C. Chang, and Q. Niu, *Rev. Mod. Phys.* **82**, 1959 (2010).
- [43] M. A. Kassem, Y. Tabata, T. Waki, and H. Nakamura, *Phys. Rev. B* **96**, 014429 (2017).
- [44] See Supplemental Material at <http://link.aps.org/supplemental/10.1103/PhysRevMaterials.4.024202> for a description of the experimental and computational parameters and methods, data analysis, and supplementary figures.
- [45] P. Vaqueiro and G. G. Sobany, *Solid State Sci.* **11**, 513 (2009).
- [46] A. K. Nayak, J. Fischer, Y. Sun, B. H. Yan, J. L. Karel, A. Komarek, C. Shekhar, N. Kumar, W. Schnelle, J. Kuebler, C. Felser, and S. S. P. Parkin, *Sci. Adv.* **2**, e1501870 (2016).
- [47] X. K. Li, L. C. Xu, L. C. Ding, J. H. Wang, M. S. Shen, X. F. Lu, Z. W. Zhu, and K. Behnia, *Phys. Rev. Lett.* **119**, 056601 (2017).

- [48] T. Suzuki, R. Chisnell, A. Devarakonda, Y. T. Liu, W. Feng, D. Xiao, J. W. Lynn, and J. G. Checkelsky, *Nat. Phys.* **12**, 1119 (2016).
- [49] S. N. Guin, K. Manna, J. Noky, S. J. Watzman, C. G. Fu, N. Kumar, W. Schnelle, C. Shekhar, Y. Sun, J. Gooth, and C. Felser, *NPG Asia Mater.* **11**, 16 (2019).
- [50] A. A. Mostofi, J. R. Yates, Y. S. Lee, I. Souza, D. Vanderbilt, and N. Marzaria, *Comput. Phys. Commun.* **178**, 685 (2008).
- [51] N. Nagaosa, J. Sinova, S. Onoda, A. H. MacDonald, and N. P. Ong, *Rev. Mod. Phys.* **82**, 1539 (2010).
- [52] J. Weischenberg, F. Freimuth, S. Blügel, and Y. Mokrousov, *Phys. Rev. B* **87**, 060406(R) (2013).